Hydrodynamic Growth of Shell Modulations in the Deceleration Phase of Spherical Direct-Drive Implosions

Introduction

The goal of inertial confinement fusion (ICF)[1,2] is to implode a spherical target to achieve fuel densities and temperatures adequate to sustain thermonuclear burn. In a spherical implosion the target is driven either by direct illumination with laser beams (direct drive)[1] or by x rays produced in a high-Z enclosure (hohlraum) containing the target (x-ray drive).[2] The unstable growth of target nonuniformities is the most significant factor disrupting the symmetry of implosions, reducing the target compression and fusion yield.[2] A direct-drive implosion begins with an acceleration phase when the laser beams ablate the shell surface directly and the capsule starts to converge. At this stage, outer-shell nonuniformities, both existing imperfections in the shell surface and imprinted due to nonuniformities in the laser drive, grow due to the acceleration-phase Rayleigh–Taylor (RT) instability.[3–16] As the shell accelerates, these front-surface perturbations feed through the shell, seeding perturbations on the inner surface. After the laser is turned off, the ablation front becomes stable and the shell starts to decelerate while continuing to converge. At stagnation, the shell stops (peak compression) and then rebounds. During the deceleration phase, the inner surface of the shell is subject to RT instability.[17–22] In addition, the modulations grow due to Bell–Plesset (BP) convergent effects[23] throughout the compression.

Experimentally, the hydrodynamic growth of target perturbations has been extensively studied using both x-ray[2–7] and direct[8–16] drive mostly in planar geometry. Both classical[3–5] and ablative[3–5,8–10] RT-instability linear growth rates have been measured using single-mode perturbations. Multimode[6,7] and broadband[16] perturbations were used to measure nonlinear saturation[24–26] and mode-coupling effects. The highly nonlinear, turbulent mixing regime of the RT-instability relevant to ICF conditions has been studied using planar geometry.[27–31] Experiments in both cylindrical[32,33] and spherical geometries[34,35] were used to measure acceleration-phase hydrodynamic growth including BP convergent effects. Small-scale mix of the highly nonlinear classical RT instability has been inferred in both x-ray[36,37] and direct-drive[38–40] spherical implosions. The deceleration-phase RT growth has been measured in spherical implosions using shell radiography by the x rays coming from the hot core emitted near peak compression.[41–43] This article presents the status of deceleration-phase hydrodynamic growth measurements and discusses future experiments.

Experimental Conditions

The modulation evolution measurements are based on differential imaging[41–43] of shells with diagnostic titanium-doped layers. Near peak compression of a spherical target implosion, when the maximum density and temperature occur, the hot, compressed core and inner surface of the shell produce strong x-ray emission. This emission can be used as a backlighter to probe the outer, colder shell. The experiments use shells with titanium-doped layers and imaging at photon energies above and below the titanium K edge. Core images at photon energies below the K edge (not absorbed by the shell) provide the spatial shape of the backlighter, while core images at photon energies above the K edge (highly absorbed by the shell's titanium) contain information about the structure of shell-areal-density modulations in the titanium-doped layer. The modulations in the cold, or absorbing, part of the shell areal density $\delta[\rho d](\mathbf{r},t)$ at time t ($\mathbf{r}$ is the spatial coordinate) are proportional to the modulation in the logarithm of the ratio of intensities of the two images at photon energies above (highly absorbing by the shell) and below (weakly absorbing by the shell) the titanium K edge.[41–43]

Figure 93.7(a) shows a schematic of a spherical target and the position of the diagnostic titanium layer used in these experiments. The targets with ~450-μm initial radii and 20-μm-thick shells, filled with 4 or 18 atm of D^{3}He gas, were imploded by 351-nm laser light using the 60-beam OMEGA laser system[44] with a 1-ns square pulse shape at a total energy of ~23 kJ. All shots were taken with laser beams smoothed by distributed phase plates (DPP's);[45] 1-THz, two-dimensional smoothing by spectral dispersion (2-D SSD);[46] and polarization smoothing (PS)[47] using birefringent wedges. The average beam-to-beam energy imbalance was ~3% in all
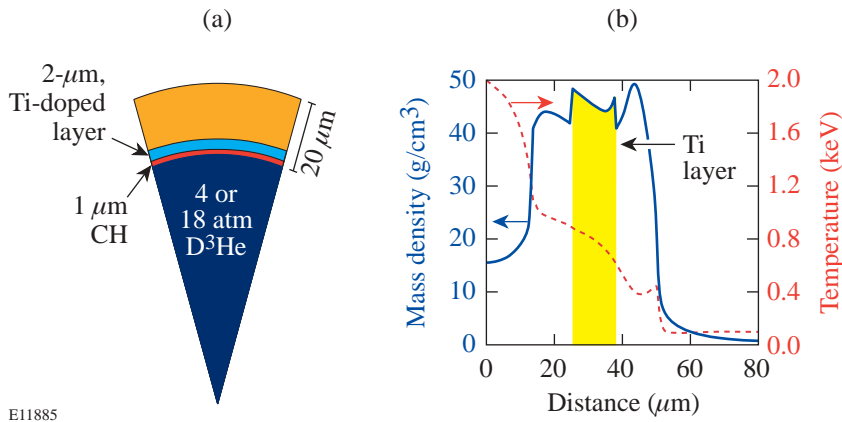
E11885

Figure 93.7
Schematic of spherical targets: (a) a 20-μm-thick shell filled with 4 or 18 atm of D^{3}He gas. (b) Simulated profiles of target density (solid line) and temperature (dashed line) at peak compression for the 18-atm target. The position of a diagnostic titanium-doped layer is shown by the yellow region.

implosions. Targets with 20-μm-thick shells filled with 4 or 18 atm of D^{3}He gas exhibit similar behavior during their laser-driven acceleration phases and therefore have similar perturbations at the beginning of the deceleration phase. Because of their differing gas-fill pressures (4 or 18 atm), these targets experience different deceleration-phase growth near peak compression.

The ~2-μm-thick, titanium-doped (~6% by atom) CH layers were offset from the inner surface by ~1 μm of pure CH. These layers were expected to be located at the unstable RT interface near peak compression. Figure 93.7(b) shows the temperature and density profiles of one of the targets [shown in Fig. 93.7(a)] with a 20-μm-thick shell filled with 18 atm of gas, calculated at peak compression by the 1-D code *LILAC*.[48] The diagnostic titanium layer (shown by the yellow region) is located on the slope of the density profile of the inner shell, where the unstable surface is located. The measured evolution of titanium-doped layer uniformity around peak compression is used to quantify the deceleration RT growth in these implosions.

The areal-density modulations in the titanium layer have been measured with differential imaging[41–43,49,50] using a framing camera. Simultaneously, the spectral evolution of core emission was captured on an x-ray streak camera. The relative areal-density modulations $\delta[\rho d]/\rho d$ in the titanium-doped layers—a measure of the shell integrity—have been obtained by normalizing the framing camera images of areal-density modulations $\delta[\rho d](\mathbf{r},t)$ to the average areal density $[\rho d](t)$ measured with the streak camera. Figure 93.8 presents images of measured areal-density modulations $\delta[\rho d](\mathbf{r},t)$ for a shot with a 20-μm-thick shell and 4 atm of D^{3}He fill around peak compression. The average titanium areal density $[\rho d](t)$ is not an accurate measure of compression in the layer because the amount of titanium atoms and ions available for absorption

can be modified by the rapidly changing core radiation and the increasing temperature in the shell around peak compression. The shell integrity $\delta[\rho d]/\rho d$ is not affected by these effects; however, an understanding of the implosion hydrodynamics requires measurements of shell-areal-density evolution along with that of the modulations.

The temporal history of the shell areal density has been inferred[51] from the spectra of primary protons from the D^{3}He fusion reaction and the evolution of the primary neutrons from the simultaneous DD reaction. The emitted primary 14.7-MeV, D^{3}He protons are slowed down by the relatively low-density fuel and the high-density shell while exiting the target. The time-integrated proton energy spectrum contains information about the target-areal-density evolution. When the measured proton energy spectrum is coupled with the neutron production history, the areal-density evolution can be inferred during the time of particle production.[51] Figure 93.9 shows the inferred temporal history of total target areal density (thick blue line) compared to a 1-D *LILAC* prediction (thin black line) in the shot with a 20-μm-thick shell and 4 atm of D^{3}He fill. The
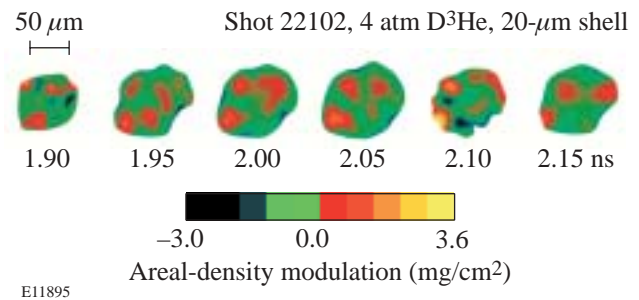
E11895

Figure 93.8
Images of areal-density modulations for a target with a 20-μm-thick shell filled with 4 atm of D^{3}He gas taken at times 1.90, 1.95, 2.00, 2.05, 2.10, and 2.15 ns.
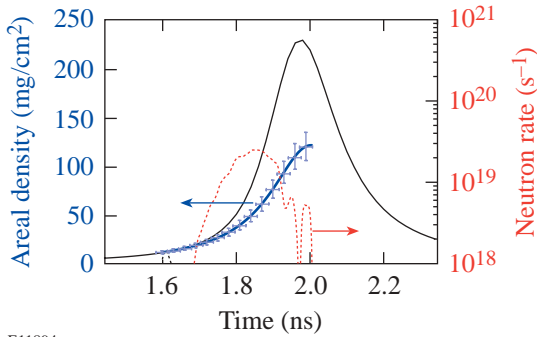
Figure 93.9
Inferred (thick blue line) and simulated (thin black line) target-areal-density evolutions for a 4-atm implosion. The measured (dotted line) neutron production history for the 4-atm implosion is from Ref. 51.

E11894

neutron-production history is shown by the dotted line for comparison. The total target areal density shown in Fig. 93.9 consists of the shell areal density (about 90% to 95%) and the gas fuel areal density (about 5% to 10%). The target (and shell) areal density grows by a factor of ~1.5 from the time of peak neutron production at ~1.9 ns to the time of peak compression at ~2.0 ns. This growth will be used below to estimate the BP contribution in the total modulation growth.

Experimental Results

Figure 93.10 shows the modulation growth inferred for two shots with 20-μm-thick shells and 4 atm of D^3He fill around peak compression. The σ_{rms} of the relative areal-density modulations $\delta[\rho d]/\rho d$ grows by a factor of ~10 during the ~200 ps around peak compression. The modulation levels are ~20% at peak neutron production (~1.9 ns) and ~50% at peak compression (~2.0 ns). Figure 93.11 shows a comparison of the non-uniformity spectra taken at peak compression for targets with 20-μm-thick shells filled with 18 atm and 4 atm of D^3He, respectively. These targets exhibit similar behavior during their laser-driven acceleration phases and therefore have similar perturbations at the beginning of the deceleration phase. Because of the different gas-fill pressures (4 or 18 atm), however, these targets experience different deceleration growths near peak compression. The power per mode of relative modulation levels $\delta[\rho d]/\rho d$ as a function of spatial frequency is shown in Fig. 93.11(a) for the more-stable 18-atm and in Fig. 93.11(b) for the more-unstable 4-atm-D^3He fills. The measured areal-density modulation levels are 23±5% and 53±11% for shots with 18-atm- and 4-atm-D^3He fills, respectively. In both spectra, measured perturbations have the highest amplitudes at spatial frequencies of about 20 to 25 mm^{-1} corresponding to spatial wavelengths of 40 to 50 μm (or a

mode number of $\ell \sim 6$), with the smallest detectable features having wavelengths of about 15 to 20 μm.

Discussion

The shell's inner-surface modulations grow due to the RT instability during the deceleration phase since the higher-density shell is slowed down by the lower-density gas of the
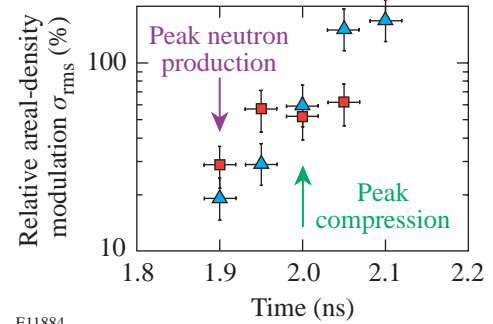
E11884

Figure 93.10
The evolution of inner-shell relative areal-density modulation σ_{rms} as a function of time for two shots [shown by triangles (shot 22102) and squares (shot 22103)] with 20-μm-thick shells filled with 4 atm of D^3He gas.
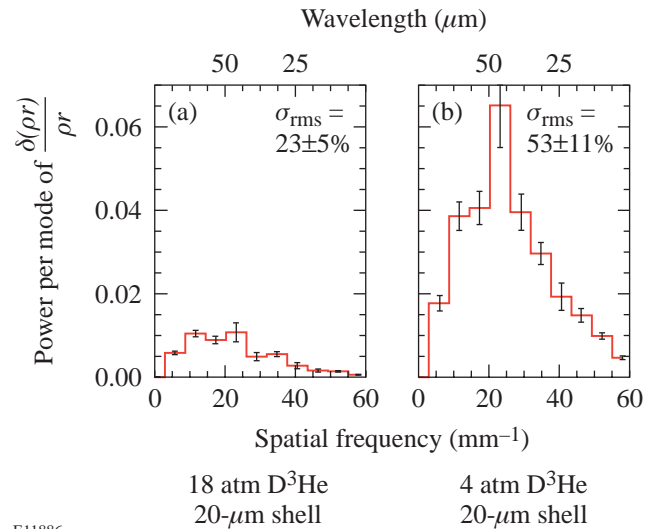
E11886

Figure 93.11
Power-per-mode spectra of relative areal-density modulations as a function of spatial frequency for 20-μm-thick shells filled with (a) 18 atm and (b) 4 atm of D^3He gas taken at peak compression and averaged over two or three shots per condition.

target core.[25–30] Unlike the acceleration-phase RT instability, where the outer-surface modulation growth is stabilized by mass ablation, the deceleration-phase RT instability is classical, with no ablative stabilization for these targets. In the linear regime of the classical RT instability, the modulation amplitude δr_1 for mode number ℓ [$\ell = kR$, where k is a modulation wave number and $R(t)$ is the radius, or position of the unstable surface] grows exponentially in time:[2]

$$\delta r_1 = \delta r_0 \, \exp\left[\sqrt{A_T(\ell/R)g t^2} \, \right], \qquad (1)$$

where A_T is the Atwood number, δr_0 is the initial perturbation amplitude, g is the deceleration, and t is time. The characteristic of the classical RT instability is the rapid growth of short-scale perturbation that quickly enters the highly nonlinear regime causing shell-density perturbations $\delta \rho$ in addition to shell-amplitude perturbations δr and shell–fuel mix. The growth of longer-wavelength perturbations can be modified by the presence of mix because the mix increases the core pressure by supplying additional material into the core. As a result, the deceleration g increases and the Atwood number A_T decreases, modifying the shell trajectory and the modulation growth.

The other factor contributing to perturbation growth is Bell–Plesset (BP) convergent effects. As the shell converges from radius R_0 (with thickness d_0 and density ρ_0) to radius R_1 (with thickness d_1 and density ρ_1), the shell modulation δr_1 grows due to BP effects[23] as

$$\delta r_1 = \delta r_0 \left(\rho_0 R_0^2\right)/\left(\rho_1 R_1^2\right) = \delta r_0 d_1/d_0.$$

The shell modulation due to BP growth is proportional to shell thickness: $\delta r \sim d$. Note that the modulation growth of shell integrity, $\delta[\rho d]/\rho d$ does not explicitly include BP effects { $\delta[\rho d]/\rho d$ due to BP effects is constant because $\delta(\rho d) \sim (\rho d)$ }; however, the convergent effects constantly modify the RT instability, which is responsible for the modulation growth.

Figure 93.12 presents schematically a physical picture of the implosions to explain the experimental data. One-dimensional *LILAC* predictions of the implosion trajectories with 4 (thin) and 18 atm (thick) of D^{3}He are shown in Fig. 93.12(a). The solid lines show the trajectories of the shell–fuel interfaces, $R(t) = R_0 - vt + g t^2/2$, for both implosions, and the dashed lines show the free-fall trajectories of these interfaces,
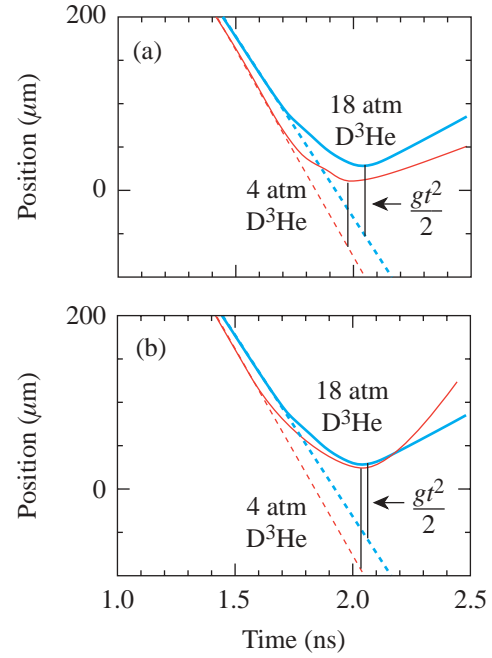
Figure 93.12
(a) *LILAC*-simulated inner-surface trajectories (solid lines) and free-fall trajectories (dashed lines) as a function of time for 20-μm-thick shells filled with 18 atm (thick) and 4 atm (thin) of D^{3}He gas. (b) The same trajectories as inferred from the experimental data.

$R_{ff}(t) = R_0 - vt$, where R_0 is the radius and v is the velocity of the inner-shell surface at the beginning of the deceleration phase. The shell velocity v is higher in the 4-atm implosion compared to the 18-atm implosion because the pressure difference between the shell and the gas is higher in the 4-atm case. The RT-growth rate of the unstable modulations in the deceleration phase of the implosion are related to the difference between inner surface and free-fall trajectories, $R(t) - R_{ff}(t) = g t^2/2$. For any mode number ℓ, the growth factor is higher in an implosion with a 4-atm fill compared to an 18-atm fill of D^{3}He because the $R(t)$ is smaller in the 4-atm implosion, and factors $g t^2/2$ are similar for both implosions at peak compression. In the experiment the expected trajectory for an 18-atm implosion is close to the 1-D *LILAC* prediction because the measured evolution of target areal density is close to 1-D. In the 4-atm implosion, however, the measured target-areal-density evolution is much lower than the 1-D prediction (as shown in Fig. 93.9) and only about 10% higher than for the 18-atm implosion.[51] The trajectories inferred from the experimental observations are shown schematically in Fig. 93.12(b) for both implosions. At peak compression the trajectories $R(t)$ are similar but the factor $g t^2/2$ is higher in the implosion with a 4-atm fill than in the 18-atm case. The

higher fuel–shell mix is responsible for the higher deceleration in the 4-atm implosion because the core pressure is increased by the addition of shell material from the mix.[38–40,52]

In the experiments, the relative areal-density modulations with spatial wavelengths ranging from about 15 to 60 μm, $\delta[\rho d]/\rho d$, grow by a factor of ~2.5 during the ~100 ps from peak neutron production (~1.9 ns) to peak compression (~2.0 ns) in the 4-atm implosion (see Fig. 93.10). The shell areal density $[\rho d]$ grows by a factor of 1.5 for the same period (see Fig. 93.9) due to the growth of both the density ρ and the thickness d; therefore, the shell modulations ($\delta r \sim d$) should grow by up to a factor of 1.5 due to BP convergent effects. The BP effects do not contribute directly to the growth of shell integrity, $\delta[\rho d]/\rho d$ therefore, the measured growth of relative areal-density modulation should be entirely due to the RT instability. In addition, the modulation growth modifies the shell trajectories leading to lower compression than predicted by 1-D in the more-unstable 4-atm implosion. At peak compression, the measured areal-density modulation levels are 23±5% and 53±11% for shots with 18-atm- and 4-atm-D^{3}He fills, respectively.

Future Experiments

The RT instability and BP growth are defined by the growth of amplitude modulations δr. In future experiments it will be necessary to measure the evolution of density along with average areal density and areal-density modulations in the titanium-doped layers to infer the evolution of amplitude modulations δr from the relative areal-density modulations $\delta[\rho d]/\rho d$. The x-ray spectrum in the titanium $1s$–$2p$ absorption region is sensitive to the density, areal density, and temperature of the layer. The time-resolved titanium absorption spectroscopy will provide the required information to better understand the unstable growth. In addition, the absorption in the titanium $1s$–$2p$ spectral region is higher by a factor of ~10 than in the region above the titanium K edge; therefore, differential imaging of shell modulations using $1s$–$2p$ absorption will be more sensitive than the results presented here.

As an example, preliminary, time-integrated shell-integrity experiments[53] based on titanium $1s$–$2p$ absorption were conducted with 20-μm-thick plastic CH shells filled with 18 atm of D^{3}He gas. The diagnostic was a 1-μm-thick, titanium-doped (~2% by atom) CH layer offset from the inner surface by ~1, 5, 7, or 9 μm of pure CH. These layers infer the shell-areal-density modulations at the inner, central, and outer parts of the shell at peak compression. Figure 93.13(a) shows the temperature and density profiles at peak compression of a representative target calculated by the 1-D code *LILAC*. At peak compression, the diagnostic titanium layer offset by 1 μm is located on the slope of the density profile at the inner shell, where the unstable surface is located. Titanium layers offset by 5 μm and 7 μm sample the central part of the shell, and the layer offset by 9 μm represents the outer part of the shell at peak compression.
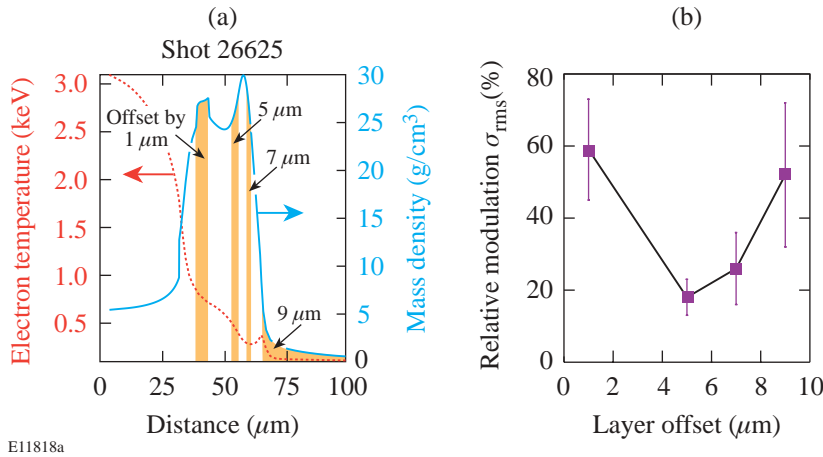

Figure 93.13
(a) *LILAC*-simulated profiles of target density and temperature at peak compression for the implosion of a 20-μm-thick shell filled with 18 atm of D^{3}He gas. The locations of titanium-doped (2% by atom) layers offset by 1, 5, 7, and 9 μm of pure CH from the inner surface are shown by the gold areas. (b) Peak-compression, relative areal-density modulation σ_{rms} as a function of the layer offset.

At peak compression, time-integrated areal-density modulations were measured using the ratios of monochromatic core images taken inside and outside of the titanium $1s$–$2p$ absorption spectral region. The relative areal-density modulation σ_{rms} was 59±14%, 18±5%, 26±10%, and 52±20% in the layers offset by 1, 5, 7, and 9 μm, respectively, as shown in Fig. 93.13(b). The modulations are highest at the inner surface (in the 1-μm-offset layer), which is unstable during the deceleration phase of the implosion near peak compression. As expected, the modulations decrease in the bulk of the shell (in the 5- and 7-μm-offset layers) but then increase at the outer surface (in the 9-μm-offset layer), which is unstable during the acceleration phase of the implosion. Time-resolved experiments based on differential imaging using the titanium $1s$–$2p$ absorption region will be conducted to study the evolution of shell nonuniformities in different parts of the shell.

As discussed in the previous section, the modulation growth of longer spatial wavelengths is modified by the presence of fuel–shell mix, which comes from the growth of shorter spatial wavelengths in the highly nonlinear phase of the classical deceleration-phase RT instability. Direct measurements of mix evolution are essential not only to quantify the short-wavelength RT growth but also to explain the observed reduction of shell compression and the modification of the longer-wavelength RT growth.

Conclusions

Shell modulation growth has been measured on targets with titanium-doped layers using differential imaging near peak compression of spherical implosions with 20-μm-thick plastic CH shells filled with 4 atm of D^3He gas. The measured perturbations have the highest amplitudes at spatial wavelengths of about 40 to 50 μm (corresponding to a mode number $\ell \sim 6$), with the shortest detectable features corresponding to wavelengths of about 15 to 20 μm. At peak neutron production, the relative areal-density modulation level $\delta[\rho d]/\rho d$ is ~20% and grows to ~50% at peak compression 100 ps later due to RT instability. For the same time period, the shell modulations grow up to about 1.5 times due to BP convergent effects. At peak compression the inner part of the shell has a higher modulation level than the bulk of the shell.

REFERENCES

1. J. Nuckolls *et al.*, Nature **239**, 139 (1972).

2. J. D. Lindl, *Inertial Confinement Fusion: The Quest for Ignition and Energy Gain Using Indirect Drive* (Springer-Verlag, New York, 1998), Chap. 6, pp. 61–82.

3. S. G. Glendinning, S. N. Dixit, B. A. Hammel, D. H. Kalantar, M. H. Key, J. D. Kilkenny, J. P. Knauer, D. M. Pennington, B. A. Remington, R. J. Wallace, and S. V. Weber, Phys. Rev. Lett. **78**, 3318 (1997).

4. K. S. Budil *et al.* Phys. Rev. Lett. **76**, 4536 (1996).

5. K. S. Budil *et al.*, Phys. Plasmas **8**, 2344 (2001).

6. B. A. Remington *et al.*, Phys. Rev. Lett. **73**, 545 (1994).

7. M. M. Marinak *et al.*, Phys. Rev. Lett. **80**, 4426 (1998).

8. J. Grun *et al.*, Phys. Rev. Lett. **58**, 2672 (1987).

9. K. Shigemori *et al.*, Phys. Rev. Lett. **78**, 250 (1997).

10. J. P. Knauer, R. Betti, D. K. Bradley, T. R. Boehly, T. J. B. Collins, V. N. Goncharov, P. W. McKenty, D. D. Meyerhofer, V. A. Smalyuk, C. P. Verdon, S. G. Glendinning, D. H. Kalantar, and R. G. Watt, Phys. Plasmas **7**, 338 (2000).

11. R. J. Taylor *et al.*, Phys. Rev. Lett. **76**, 1643 (1996).

12. D. H. Kalantar, M. H. Key, L. B. Da Silva, S. G. Glendinning, B. A. Remington, J. E. Rothenberg, F. Weber, S. V. Weber, E. Wolfrum, N. S. Kim, D. Neely, J. Zhang, J. S. Wark, A. Demir, J. Lin, R. Smith, G. J. Tallents, C. L. S. Lewis, A. MacPhee, J. Warwick, and J. P. Knauer, Phys. Plasmas **4**, 1985 (1997).

13. H. Azechi *et al.*, Phys. Plasmas **4**, 4079 (1997).

14. C. J. Pawley *et al.*, Phys. Plasmas **6**, 565 (1999).

15. T. R. Boehly, V. N. Goncharov, O. Gotchev, J. P. Knauer, D. D. Meyerhofer, D. Oron, S. P. Regan, Y. Srebro, W. Seka, D. Shvarts, S. Skupsky, and V. A. Smalyuk, Phys. Plasmas **8**, 2331 (2001).

16. V. A. Smalyuk, T. R. Boehly, D. K. Bradley, V. N. Goncharov, J. A. Delettrez, J. P. Knauer, D. D. Meyerhofer, D. Oron, and D. Shvarts, Phys. Rev. Lett. **81**, 5342 (1998).

17. H. Sakagami and K. Nishihara, Phys. Rev. Lett. **65**, 432 (1990).

18. R. P. J. Town and A. R. Bell, Phys. Rev. Lett. **67**, 1863 (1991).

19. M. M. Marinak *et al.*, Phys. Plasmas **3**, 2070 (1996).

20. V. Lobatchev and R. Betti, Phys. Rev. Lett. **85**, 4522 (2000).

21. M. C. Herrmann, M. Tabak, and J. D. Lindl, Phys. Plasmas **8**, 2296 (2001).

22. R. Betti, K. Anderson, V. N. Goncharov, R. L. McCrory, D. D. Meyerhofer, S. Skupsky, and R. P. J. Town, Phys. Plasmas **9**, 2277 (2002).

23. M. S. Plesset and T. P. Mitchell, Q. Appl. Math. **13**, 419 (1956).

24. S. W. Haan, Phys. Rev. A **39**, 5812 (1989).

25. S. W. Haan, Phys. Fluids B **3**, 2349 (1991).

26. M. J. Dunning and S. W. Haan, Phys. Plasmas **2**, 1669 (1995).

27. D. L. Youngs, Physica D **37**, 270 (1989).

28. K. I. Read, Physica **12D**, 45 (1984).

29. G. Dimonte and M. Schneider, Phys. Rev. E **54**, 3740 (1996).

30. G. Dimonte, Phys. Plasmas **6**, 2009 (1999).

31. M. B. Schneider, G. Dimonte, and B. Remington, Phys. Rev. Lett. **80**, 3507 (1998).

32. W. W. Hsing *et al.*, Phys. Plasmas **4**, 1832 (1997).

33. D. L. Tubbs, C. W. Barnes, J. B. Beck, N. M. Hoffman, J. A. Oertel, R. G. Watt, T. Boehly, D. Bradley, P. Jaanimagi, and J. Knauer, Phys. Plasmas **6**, 2095 (1999).

34. C. Cherfils *et al.*, Phys. Rev. Lett. **83**, 5507 (1999).

35. S. G. Glendinning *et al.*, Phys. Plasmas **7**, 2033 (2000).

36. T. R. Dittrich *et al.*, Phys. Rev. Lett. **73**, 2324 (1994).

37. M. D. Cable *et al.*, Phys. Rev. Lett. **73**, 2316 (1994).

38. D. D. Meyerhofer, J. A. Delettrez, R. Epstein, V. Yu. Glebov, V. N. Goncharov, R. L. Keck, R. L. McCrory, P. W. McKenty, F. J. Marshall, P. B. Radha, S. P. Regan, S. Roberts, W. Seka, S. Skupsky, V. A. Smalyuk, C. Sorce, C. Stoeckl, J. M. Soures, R. P. J. Town, B. Yaakobi, J. D. Zuegel, J. Frenje, C. K. Li, R. D. Petrasso, D. G. Hicks, F. H. Séguin, K. Fletcher, S. Padalino, M. R. Freeman, N. Izumi, R. Lerche, T. W. Phillips, and T. C. Sangster, Phys. Plasmas **8**, 2251 (2001).

39. P. B. Radha, J. Delettrez, R. Epstein, V. Yu. Glebov, R. Keck, R. L. McCrory, P. McKenty, D. D. Meyerhofer, F. Marshall, S. P. Regan, S. Roberts, T. C. Sangster, W. Seka, S. Skupsky, V. Smalyuk, C. Sorce, C. Stoeckl, J. Soures, R. P. J. Town, B. Yaakobi, J. Frenje, C. K. Li, R. Petrasso, F. Séguin, K. Fletcher, S. Padalino, C. Freeman, N. Izumi, R. Lerche, and T. W. Phillips, Phys. Plasmas **9**, 2208 (2002).

40. S. P. Regan, J. A. Delettrez, F. J. Marshall, J. M. Soures, V. A. Smalyuk, B. Yaakobi, V. Yu. Glebov, P. A. Jaanimagi, D. D. Meyerhofer, P. B. Radha, W. Seka, S. Skupsky, C. Stoeckl, R. P. J. Town, D. A. Haynes, Jr., I. E. Golovkin, C. F. Hooper, Jr., J. A. Frenje, C. K. Li, R. D. Petrasso, and F. H. Séguin, Phys. Rev. Lett. **89**, 085003 (2002).

41. B. Yaakobi, V. A. Smalyuk, J. A. Delettrez, F. J. Marshall, D. D. Meyerhofer, and W. Seka, Phys. Plasmas **7**, 3727 (2000).

42. V. A. Smalyuk, V. N. Goncharov, J. A. Delettrez, F. J. Marshall, D. D. Meyerhofer, S. P. Regan, and B. Yaakobi, Phys. Rev. Lett. **87**, 155002 (2001).

43. V. A. Smalyuk, J. A. Delettrez, V. N. Goncharov, F. J. Marshall, D. D. Meyerhofer, S. P. Regan, T. C. Sangster, R. P. J. Town, and B. Yaakobi, Phys. Plasmas **9**, 2738 (2002).

44. T. R. Boehly, D. L. Brown, R. S. Craxton, R. L. Keck, J. P. Knauer, J. H. Kelly, T. J. Kessler, S. A. Kumpan, S. J. Loucks, S. A. Letzring, F. J. Marshall, R. L. McCrory, S. F. B. Morse, W. Seka, J. M. Soures, and C. P. Verdon, Opt. Commun. **133**, 495 (1997).

45. Y. Lin, T. J. Kessler, and G. N. Lawrence, Opt. Lett. **20**, 764 (1995).

46. S. P. Regan, J. A. Marozas, J. H. Kelly, T. R. Boehly, W. R. Donaldson, P. A. Jaanimagi, R. L. Keck, T. J. Kessler, D. D. Meyerhofer, W. Seka, S. Skupsky, and V. A. Smalyuk, J. Opt. Soc. Am. B **17**, 1483 (2000).

47. T. R. Boehly, V. A. Smalyuk, D. D. Meyerhofer, J. P. Knauer, D. K. Bradley, R. S. Craxton, M. J. Guardalben, S. Skupsky, and T. J. Kessler, J. Appl. Phys. **85**, 3444 (1999).

48. J. Delettrez, R. Epstein, M. C. Richardson, P. A. Jaanimagi, and B. L. Henke, Phys. Rev. A **36**, 3926 (1987).

49. V. A. Smalyuk, T. R. Boehly, L. S. Iwan, T. J. Kessler, J. P. Knauer, F. J. Marshall, D. D. Meyerhofer, C. Stoeckl, B. Yaakobi, and D. K. Bradley, Rev. Sci. Instrum. **72**, 635 (2001).

50. V. A. Smalyuk, B. Yaakobi, J. A. Delettrez, F. J. Marshall, and D. D. Meyerhofer, Phys. Plasmas **8**, 2872 (2001).

51. V. A. Smalyuk, P. B. Radha, J. A. Delettrez, V. Yu. Glebov, V. N. Goncharov, D. D. Meyerhofer, S. P. Regan, S. Roberts, T. C. Sangster, J. M. Soures, C. Stoeckl, J. A. Frenje, C. K. Li, R. D. Petrasso, and F. H. Séguin, "Time-Resolved Areal-Density Measurements with Proton Spectroscopy in Spherical Implosions," to be published in Physical Review Letters.

52. C. K. Li, F. H. Séguin, J. A. Frenje, S. Kurebayashi, R. D. Petrasso, D. D. Meyerhofer, J. M. Soures, J. A. Delettrez, V. Yu. Glebov, P. B. Radha, F. J. Marshall, S. P. Regan, S. Roberts, T. C. Sangster, and C. Stoeckl, Phys. Rev. Lett. **89**, 165002 (2002).

53. V. A. Smalyuk, S. B. Dumanis, F. J. Marshall, J. A. Delettrez, D. D. Meyerhofer, S. P. Regan, T. C. Sangster, B. Yaakobi, and J. A. Koch, to be published in Physics of Plasmas.